PHYSICAL REVIEW B **87**, 125108 (2013)

Direction-selective emission with small angular divergence from a subwavelength aperture using radiative waveguide modes

Wook-Jae Lee, Jong-Bum You, Kyungmook Kwon, Byounghun Park, and Kyoungsik Yu[*]
Department of Electrical Engineering, KAIST, Daejeon 305-701, Republic of Korea

(Received 3 August 2012; revised manuscript received 7 February 2013; published 6 March 2013)

We investigate experimentally and theoretically the highly direction-selective emission with small angular divergence in a metal-dielectric-metal structure with a subwavelength metal aperture layer. The thicknesses of the dielectric layer and top metal layer play important roles in controlling the emission direction and angular divergence, respectively. Dispersion curve calculations based on the transfer matrix method indicate that the directional emission is mediated by radiative waveguide modes. We show that the directional emission in a metal-dielectric-metal structure is independent of the polarization of the incident light in contrast to plasmonic beaming structures, such as a subwavelength aperture surrounded by surface corrugations with a strong polarization dependence.

DOI: 10.1103/PhysRevB.87.125108 PACS number(s): 42.25.Bs, 42.25.Fx, 78.66.Bz, 79.60.Dp

I. INTRODUCTION

Light passing through a subwavelength aperture is usually diffracted in all directions and propagates with very small power.[1] These features have been considered as important constraints in controlling light emission and propagation. In 2002, Lezec and colleagues reported the light beaming based on surface waves generated by surface corrugations around the metal apertures.[2] The presence of collimated light from a subwavelength metal aperture has stimulated a lot of research on the fundamental theories[3–8] as well as various applications of this phenomenon for passive and active optical devices such as plasmonic antennas[9–12] and divergence-controlled lasers.[13,14] The design space for the corrugated apertures, however, is quite diverse and complicated.[15] Multiple geometrical parameters, such as the period, width, and depth of corrugations, the distance between the first corrugation and the aperture, and the width and thickness of the aperture, need to be carefully chosen from the working wavelength for optimal beaming performance beyond the diffraction limit. The symmetry of the structure and profiles of the corrugations is also important because such variables determine the distribution of the surface waves that interfere with the incident light to result in the directional emission.[4,7,15] Furthermore, the corrugated aperture dimensions heavily rely on the illumination wavelength (λ_0) because the corrugation periods for directional emission should be comparable to or smaller than the operation wavelength. Consequently, the beaming structures around the subwavelength aperture need to be fabricated by sophisticated fabrication processes and do not scale well with the working wavelengths.

In recent studies, a dielectric multilayer structure was proposed to facilitate directive emission from a single oriented molecule.[16,17] Although this structure is insensitive to the emitter wavelength and provides nearly ideal collection efficiencies, the emission direction around the normal to a dielectric layer cannot be tailored in a narrow angular range and the emitted photons having angles above $\arcsin(n_2/n_1)$ do not couple to the free space due to the total internal reflection (where n_1 and n_2 are refractive index of the substrate and the free space, respectively). Epsilon-near-zero metamaterials have also been shown to control the emission direction into the free space within a narrow radiation angle around the normal to the metamaterial surface.[18] Anisotropic metamaterials have also been proposed to achieve off-axis emission properties.[19] These approaches are required to provide the desired optical constants of periodic composite structures at a specific wavelength when such structures are composed of metal-dielectric stacks or metallic wires[20,21] with dimensions much smaller than the operating wavelength.[22] As the operating wavelength decreases, however, the optical constants of such thin or small structures are difficult to design and control precisely in practice.[23–25]

In this paper, we propose to use a metal-dielectric-metal (MDM) structure, which consists of three layers (the subwavelength metal aperture layer, the dielectric core layer, and the top metal layer) for direction-selective emission (DSE) with small angular divergence without any corrugated lateral structures. To the best of our knowledge, the DSE property from a subwavelength aperture in the MDM structure has not yet been studied in detail at optical frequencies. The proposed structure shows not only a highly directional emission but also a remarkable control of the emission direction by varying the distance between the aperture and top metal layer. We demonstrate theoretically and experimentally that the DSE in the MDM structure can be explained as a result of excitation of radiative waveguide modes (RWMs). Further, we observed that the DSE can be achieved irrespective of the polarization of the incident light.

Note that although we focused on the light source with a 365-nm wavelength in order to evaluate the performance of the proposed structure without the short-period corrugation of the order of the illumination wavelengths, the same principle can be applied to wide wavelength ranges because the RWMs supported by the MDM structure can be observed at various wavelengths.

II. THEORETICAL APPROACH FOR DIRECTION-SELECTIVE EMISSION SYSTEM

A. Radiative waveguide mode

In a conventional beaming structure surrounded by periodic surface corrugations, the directional beaming phenomenon

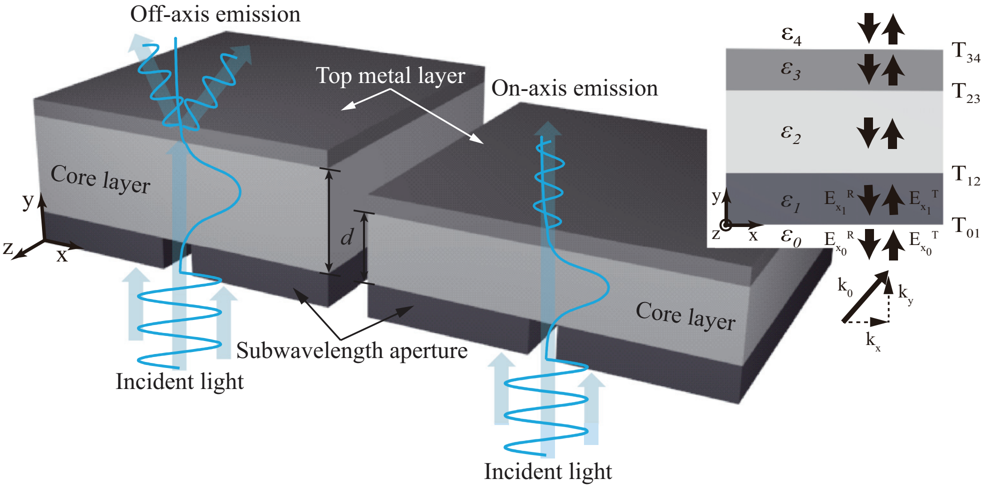

FIG. 1. (Color online) Schematic diagrams of the DSE processes from subwavelength metal apertures. The thickness of the dielectric core layer is denoted by d. The x, y, and z axes show the Cartesian coordinate used in this work. Shown in the inset is schematic geometry of the the five-layered system. T_{01}, T_{12}, T_{23}, and T_{34} indicate the transfer matrices at each interface.

can be stated whereby the surface wave which propagates on the corrugated surface, after diffraction from a subwavelength aperture, is converted and redirected into the radiating wave in a specific direction with small divergence angle by matching the wave-vector components along the aperture plane.[7]

An alternative and simpler way to obtain the directional emission is to use the nature of RWMs. It is well known that the mode power of the RWM can travel outside the waveguide and the radiation angle of the RWM can be easily controlled by changing the waveguide core thickness. When, in other words, a well-defined RWM is excited, the radiated field out of the waveguide can couple to free space modes.[26] Thus, the RWM is a good candidate for the directional emission without any surface corrugations on the metal surface. To accomplish the directional emission using the RWM, we employed a metal-clad waveguide structure composed of a subwavelength metal aperture layer, a dielectric core layer, and a top metal layer as schematically described in Fig. 1.

B. Dispersion curve using a transfer matrix method

We start by calculating the dispersion curve of the suggested MDM structure for transverse magnetic (TM) polarization (i.e., the magnetic field is perpendicular to the plane of incidence). Although there are many methods for determining the dispersion curve, we used the transfer matrix method (TMM)[27] due to its advantages that can describe the transmission coefficients for each spatial frequency (k_x) as schematically shown in the inset of Fig. 1. Once the transmission coefficient is obtained as a function of the spatial frequency component k_x, we can plot the dispersion curves of the RWM (propagating or above the light line) as well as the waveguide modes (exponentially decaying or below the light line) as a function of the incident wavelength. For the sake of simplicity, we approximate a subwavelength metal aperture layer to a planar metal layer without an aperture for TMM calculations. We then validate our scheme by comparing the result of finite-difference time-domain (FDTD) simulations.

We consider a plane-wave incident with an arbitrary incident angle and a five-layer thin-film system (the MDM structure bounded by dielectrics) as seen in the inset of Fig. 1. The transfer matrix can be expressed in terms of the electric field for the TM-polarized plane wave using the boundary conditions

$$E_{\text{out}} = T E_{\text{in}}, \tag{1}$$

where E_{out} and E_{in} are the electric field components of outgoing and incoming waves, respectively. According to Ref. 27, we can derive the transfer matrix (T_{lm}) for the x component of the electric field in a multilayer system

$$\begin{bmatrix} E_{x_1}^T \\ E_{x_1}^R \end{bmatrix} = \frac{k_{y_m}}{2\epsilon_m} \begin{bmatrix} \frac{\epsilon_l}{k_{y_l}} + \frac{\epsilon_m}{k_{y_m}} & \frac{\epsilon_m}{k_{y_m}} - \frac{\epsilon_l}{k_{y_l}} \\ \frac{\epsilon_m}{k_{y_m}} - \frac{\epsilon_l}{k_{y_l}} & \frac{\epsilon_l}{k_{y_l}} + \frac{\epsilon_m}{k_{y_m}} \end{bmatrix} \begin{bmatrix} E_{x_0}^T \\ E_{x_0}^R \end{bmatrix} = T_{\text{lm}} \begin{bmatrix} E_{x_0}^T \\ E_{x_0}^R \end{bmatrix}, \tag{2}$$

where ϵ_l and ϵ_m are the optical constants on each side of the interface and $k_{y_l} = \sqrt{\epsilon_l k_0^2 - k_x^2}$ for $l = 0,1,2,3$ and $m = 1,2,3,4$.

The transfer matrix can be extended from the interface location at the y origin to an arbitrary position of y,

$$T(y)_{\text{lm}} = \begin{bmatrix} e^{-ik_{y_m}y} & 0 \\ 0 & e^{ik_{y_m}y} \end{bmatrix} T(0)_{\text{lm}} \begin{bmatrix} e^{-ik_{y_l}y} & 0 \\ 0 & e^{ik_{y_l}y} \end{bmatrix}, \tag{3}$$

for $l = 0,1,2,3$ and $m = 1,2,3,4$.

If we consider the incident, reflected, and transmitted electric field, Eq. (2) can be rearranged by

$$\begin{bmatrix} t \\ 0 \end{bmatrix} = \begin{bmatrix} T^{11} & T^{12} \\ T^{21} & T^{22} \end{bmatrix} \begin{bmatrix} 1 \\ r \end{bmatrix}, \tag{4}$$

where t and r are the transmission and reflection coefficients, respectively. From Eq. (4), the transmission intensity at an arbitrary position y of the final layer is given by

$$|t|^2 = \left| \frac{T^{11}T^{22} - T^{12}T^{21}}{T^{22}} \right| e^{ik_{y_4}y}. \tag{5}$$

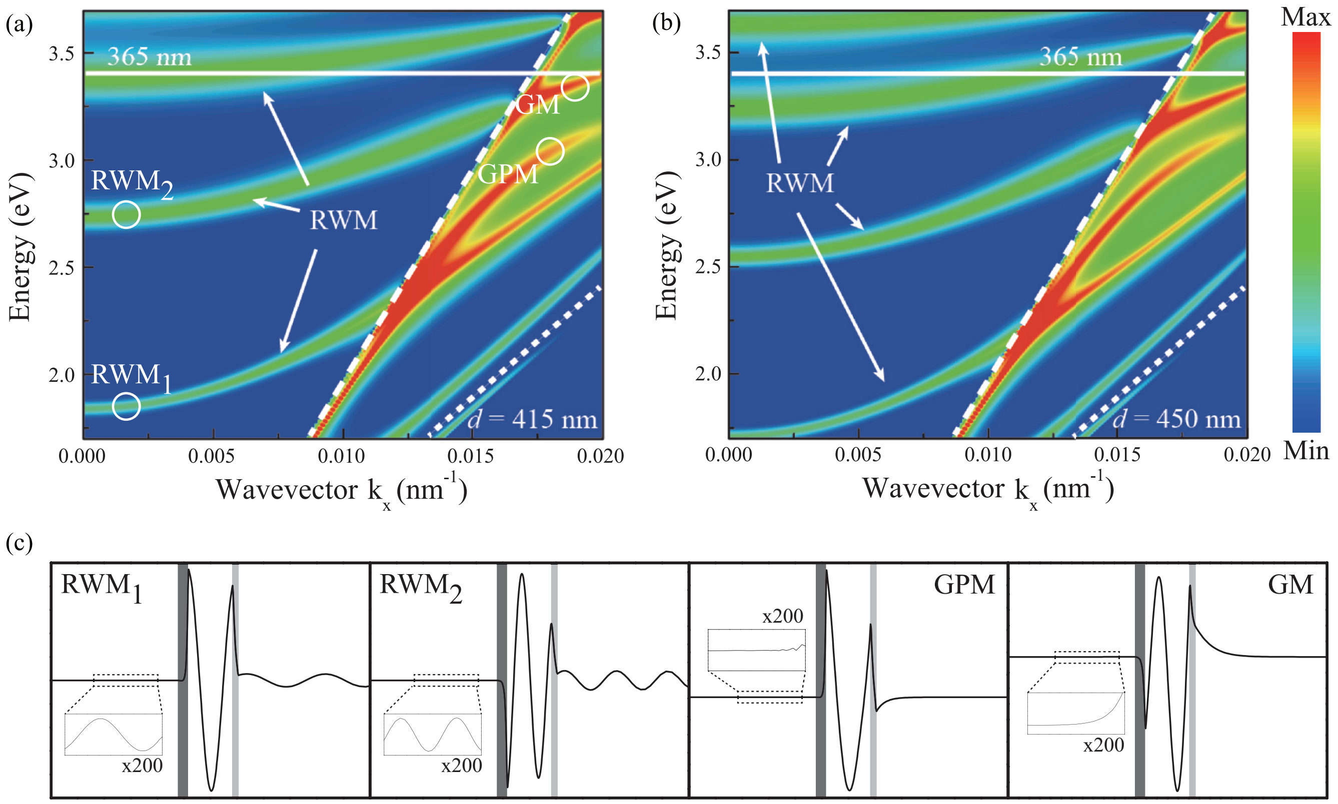

FIG. 2. (Color online) Dispersion curves for the proposed MDM structure for (a) $d = 415$ nm and (b) $d = 450$ nm. Dispersion relations are obtained from the TMM. False color indicates the transmitted light intensity on a log scale through the MDM structure. Horizontal solid lines indicate the considered incident wavelength in this paper. Dashed and dotted lines are the light lines for free space and PMMA layer, respectively. (c) H_z field profiles corresponding to the RWM, guided plasmonic mode (GPM), and GM as a function of the distance in the y direction. Dark and bright gray regions account for the aluminum and silver layers in the MDM structure, respectively. Insets show the magnified field amplitude (200 times).

By choosing a suitable position y, we can obtain the dispersion curve for both the guided mode (GM) and the RWM as shown in Fig. 1. The amplitude of the transmitted spatial frequency at a certain wavelength can be also converted into the angular distribution of the transmitted light. Thus, the TMM is a simple and effective way to not only determine the dispersion curve but also show the emission direction and angular divergence.

We designed the MDM structure composed of three layers: aluminum-dielectric-silver. The aluminum film with a thickness of 100 nm was chosen as an aperture layer to prevent direct transmission of the illumination light. The silver film with a thickness of 50 nm was adopted as a top metal layer for moderate transmission and good directivity. The optical constants of aluminum and silver are fitted from Palik's data.[28] In our work, the polymethyl methacrylate (PMMA[29]) material is employed as a dielectric core layer between the aluminum aperture layer and the silver film, but other dielectric materials can also be used to obtain the DSE effects.

Figures 2(a) and 2(b) display the calculated dispersion curves for two different PMMA core-layer thicknesses as a function of the wave-vector components along the aperture plane (spatial frequency k_x). The transmission intensity through the MDM structure is computed at the final metal-dielectric (ϵ_3-ϵ_4) interface and represented in color. Red and blue colors correspond to the maximum and minimum intensity, respectively. Our calculation using the TMM reveals that the MDM structure supports several RWMs as explained in previous works,[30–32] and their dispersion relation depends on the PMMA core thickness. This result implies that the DSE can be observed at various wavelengths using the RWM and can be finely tuned by changing the thickness of the dielectric core.

In order to understand the DSE from the dispersion curve, we plot in Fig. 3(a) the calculated angular transmission distributions at 365-nm wavelength as a function of the transmission angle (θ) which is given by $\theta = \arcsin(k_x/k_0)$ where $k_0 = 2\pi/\lambda_0$. Figure 3(a) shows that the value of the transmission peak, in the case of $d = 450$ nm, is about 1.4 times higher compared with the case of $d = 415$ nm. The transmitted light is highly confined around 0° and ±38° for $d = 415$ nm and 450 nm, respectively. It is clearly shown that highly directional propagation with small angular divergence can be obtained while the emission direction is regulated by the core layer thickness d. Figure 3(b) shows that the beam divergence angles decrease with thicker silver films where the transmission intensities are normalized by the peak intensities at each PMMA core thickness. The maximum transmission angle remained at the same value even with the change of top silver film thickness. We therefore can independently

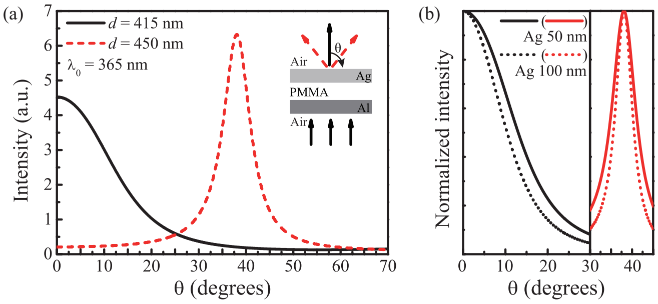

FIG. 3. (Color online) (a) Angular transmission profiles for two different PMMA core thicknesses at the 365-nm wavelength. (b) Angular transmission profiles when the top metal layer thickness is changed. Black and red lines indicate $d = 415$ nm and 450 nm, respectively. Thicker Ag films lead to smaller divergence.

tailor both the emission direction and angular divergence by changing the dielectric core and/or top metal layer thicknesses.

C. Finite-difference time-domain simulations

Next we performed two-dimensional FDTD simulations using a commercial software package (Lumerical FDTD Solutions) to numerically verify the performance of the MDM structure using the TMM. The simulation conditions are essentially the same with TMM calculations. The periodic boundary conditions are adopted in the horizontal direction and the perfectly matched layer absorbing boundary condition is employed in the vertical direction. A grid size of 5 nm is used. We considered a one-dimensional subwavelength slit with a 90-nm width and a normally incident plane wave with TM polarization.

When a plane wave is incident on a slit layer, the transmitted light through a subwavelength slit excites the RWM and the GM. Figures 4(a) and 4(b) depict the transmission profiles from the FDTD simulations for different PMMA core-layer thicknesses. On- and off-axis collimated beams associated with the RWM were obtained for $d = 415$ nm and 450 nm, respectively, and the GMs propagating along the PMMA core layer were also observed. The angular transmission profiles along the x axis at $y = 10$ μm are plotted in Fig. 4(c). The transmission peaks are observed around 0° and ±41° for $d = 415$ nm and 450 nm, respectively. The value of the transmission peak for the core layer thickness $d = 450$ nm is about 1.45 times higher than in the case of $d = 415$ nm. Figure 4(c) demonstrates that the angular distributions obtained from the FDTD results agree very well with the TMM calculations. The slight difference of the peak position between the TMM and FDTD results for $d = 450$ nm can be attributed to the aperture effect because a subwavelength slit layer in FDTD simulation is considered to be a planar metal layer without an aperture in the TMM calculation. We also calculated, using the FDTD simulations, the field profiles (H_z) along the y axis of the MDM structure at $d = 415$ nm [see Fig. 2(c)]. The distributions of the field clearly show the profiles of the RWM and the GM.

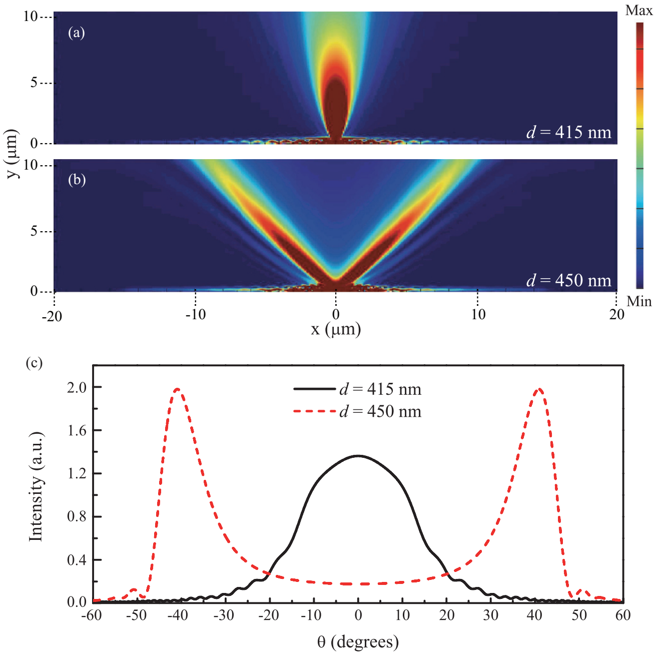

FIG. 4. (Color online) [(a) and (b)] FDTD simulation results for the same conditions with TMM calculations. (c) Angular transmission profiles obtained at $y = 10$ μm for (a) and (b).

III. EXPERIMENTS

A. Experimental setup and sample preparation

We verify our theory by measuring the far-field images from the subwavelength apertures. We fabricated several samples with subwavelength slits whose apertures were defined by electron beam lithography in 100-nm-thick aluminum film deposited on a glass substrate. A scanning electron micrograph (SEM) of a typical subwavelength slit is shown in the inset of Fig. 5(a). The width and height of the slit are 90 and 20 000 nm, respectively. The slit height was selected to be long enough to neglect diffraction effects along the z axis. The PMMA core layer was formed by multiple spin coatings in order to minimize the surface roughness and then partially etched by oxygen plasma ashing until the desired thickness was reached. The PMMA layer thicknesses were rigorously confirmed by a surface profiler (Veeco Dektak6M). The root-mean-square surface roughness was measured to be <1 nm near the slit area by atomic force microscopy. Both the aluminum and silver films were deposited using electron beam evaporation. Incident light with a center wavelength at 365 nm (Thorlabs M365L2) is illuminated perpendicularly to the slit, and the images of the transmitted light intensity were measured using an optical microscope (Olympus BX51M) with a 100× objective lens (Olympus LMPlanFL, NA = 0.8) and a charge-coupled-device camera (Jenoptik ProgRes MFcool). The optical images were observed at a distance of 10 μm (y axis) above the aperture surface. The experimental arrangement is shown in Fig. 5(a).

B. Experimental results

We then compared the measured far-field images of a bare slit and a slit with the MDM structure. Figure 5(b) shows

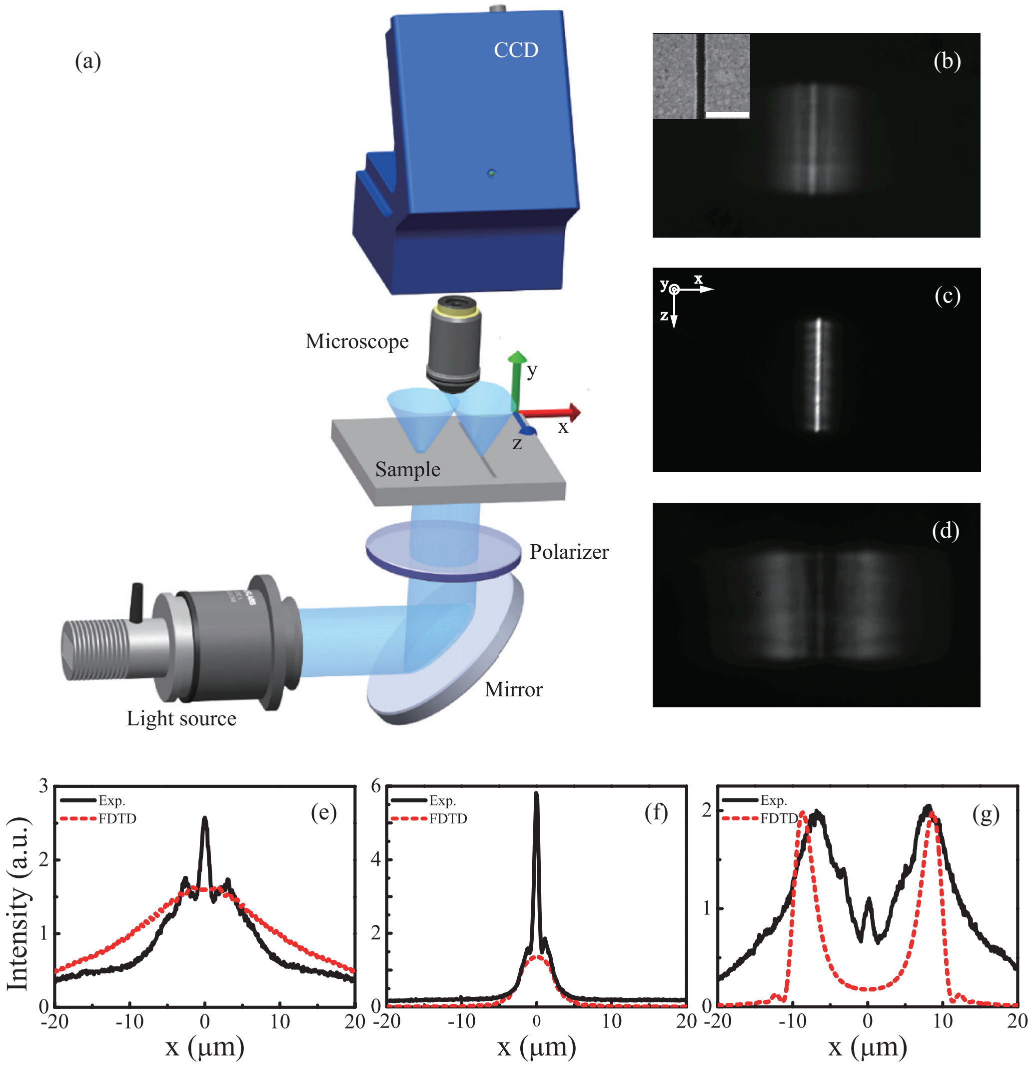

FIG. 5. (Color online) (a) Schematic picture of the experimental setup. (b) Optical image from a bare subwavelength slit without a metal-dielectric film at $y = 10$ μm. An SEM of a typical subwavelength slit with a 90-nm width is shown in the inset. The white scale bar represents 500 nm. Optical images obtained at $y = 10$ μm for (c) $d = 415$ nm and (d) $d = 450$ nm are shown for comparison. [(e)–(g)] Cross sections of the transmission intensity along the x axis for (b), (c), and (d), respectively. Black solid curves are the experimental data from the images while red dashed curves are from the FDTD simulations.

the optical image of the transmitted light through the bare aluminum slit without the PMMA core layer and the metal film. As expected, the measured optical image exhibits wide spatial distributions along the x axis. The optical image in Fig. 5(c) emerging from a sample with 415-nm-thick PMMA core and 50-nm-thick silver film displays a narrower central beam than the transmitted light through the bare slit in Fig. 5(b). Figure 5(d) shows the off-axis directional beaming with an emission angle of 37° via the 450-nm-thick PMMA core and 50-nm-thick silver film. The optical images with the proposed MDM structure were captured under the same exposure conditions except that the bare slit image of Fig. 5(b) was attenuated by $1/20$. These results together with the theoretical calculations confirm that the small angular divergence and the emission direction of the transmitted light can be controlled simply by the metal film and the dielectric core thicknesses. In Figs. 5(e)–5(g), the transmission profiles along the x axis for the experimental (black solid lines) and numerical results (red dashed lines) are compared. The intensity profiles from the FDTD simulations are scaled by the same scaling parameter in Figs. 5(f) and 5(g). The discrepancy between the peak positions of the calculated and measured data as shown in Fig. 5(g) originates in the different PMMA-core-layer thickness within a range of ±2.5 nm. The large peaks in the middle of the intensity profiles are due to the scattered out-of-focus light from the slit aperture and the background noise from the out-of-focus blur because of the nonzero depth of focus of the objective. For off-axis directional beaming, a smaller amount of such out-of-focus light (center peak) is observed because of strong attenuation of the transmitted light in the central direction.

To further investigate the directional beaming using RWM, we turn our attention to two-dimensional apertures (i.e., holes in a metal film). We prepared a sample with a circular aperture whose diameter is around 60 nm, as shown in the inset of Fig. 6(a). Figure 6(a) shows the measured optical images at

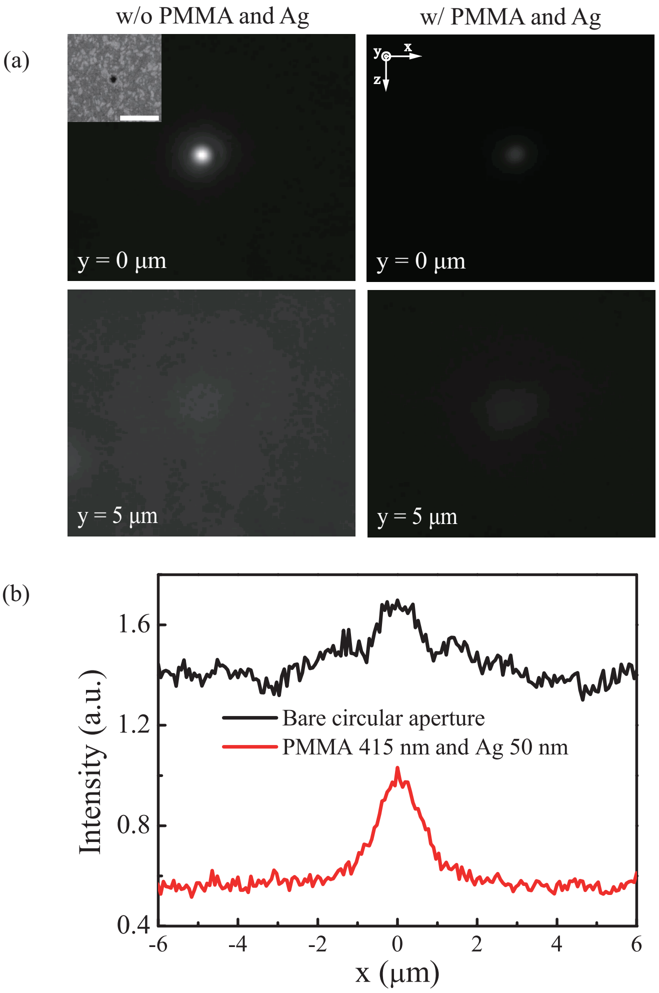

FIG. 6. (Color online) (a) Optical images at $y = 0$ μm and 5 μm passing through a subwavelength circular aperture without and with the 415-nm-thick PMMA core and the 50-nm-thick silver film. The inset shows an SEM of a subwavelength circular aperture with a 60-nm diameter. The white scale bar represents 500 nm. (b) Cross sections of the transmission intensity profiles along the x axis at $y = 5$ μm in the case of without (black curve) and with (red curve) the PMMA layer and the silver film.

$y = 0$ μm (aperture plane) and at $y = 5$ μm above the aperture surface without and with the MDM structure. The intensity of the optical images without the proposed structure at $y = 5$ μm was attenuated by about one-third as compared with the optical image with the proposed structure. As described in Fig. 6(a), the emission from a circular aperture without the PMMA core layer and the metal film is too divergent to be directly observed at $y = 5$ μm if the out-of-focus contribution is removed. On the other hand, a well-collimated beam is generated when the 415-nm-thick PMMA core and the 50-nm-thick silver film are added on a circular aperture. Figure 6(b) depicts the intensity distributions as a function of the distance in the x direction. The red curve shows a clear well-defined peak of the directional beam even if we consider the background noise in the center arising from the out-of-focus light, whereas the black curve does not show such features except for the low-contrast center peak due to the out-of-focus light. We believe that these results can be used in a number of applications that take advantage of the DSE from two-dimensional subwavelength metal apertures. Note that we could not observe the off-axis directional beaming for the 450-nm-thick PMMA core mainly because of the angular spreading of the transmitted light with weak intensity. We expect, however, that the off-axis directive emission can be obtained using thinner metal layers.

IV. DISCUSSION

A. Wavelength dependence of directional beaming

Until now, we have presented the DSE at a 365-nm illumination wavelength where silver film is transparent. The DSE performance at different illumination wavelengths has been studied in Fig. 7 using the TMM calculations. We considered that the silver layers with the same thickness were chosen as the aperture and top metal layers. The thicknesses of the PMMA cores were selected to produce the on-axis collimated beams for the corresponding input wavelengths. The transmission intensity is normalized to the intensity of the incident wave. Figure 7 exhibits that the high transmission with small angular divergence can be observed for higher wavelength by varying the thicknesses of the metal layers. Therefore, the DSE phenomenon with small angular divergence can be obtained independent of the operating wavelength. FDTD calculations show similar results (not shown here).

B. Ability to modulate the transmitted light

An important advantage of our proposed structure is its ability to tune the emission direction by varying the thickness and/or the refractive index of the dielectric core layer. Such parameters can be readily controlled by thermo- and electro-optic effects.[33–37] Moreover, we can directly use the metal-clad structure as electrodes for thermal heating or electrical modulation in the MDM structure.

Figures 8(a) and 8(b) show the DSE behaviors with respect to the thickness and the refractive-index change of the PMMA core layer at the illumination wavelength of 632.8 nm, respectively. The position and value of the transmission peak can be sensitively controlled by changing the thickness of the

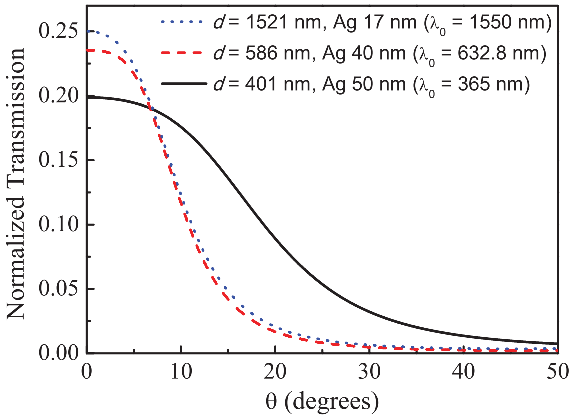

FIG. 7. (Color online) Normalized angular transmission profiles obtained by the TMM calculations for illumination wavelength of 365, 632.8, and 1550 nm. Thicknesses of the PMMA core are 401, 586, and 1521 nm, respectively. Thicknesses of both the aperture and top metal layers are the same.

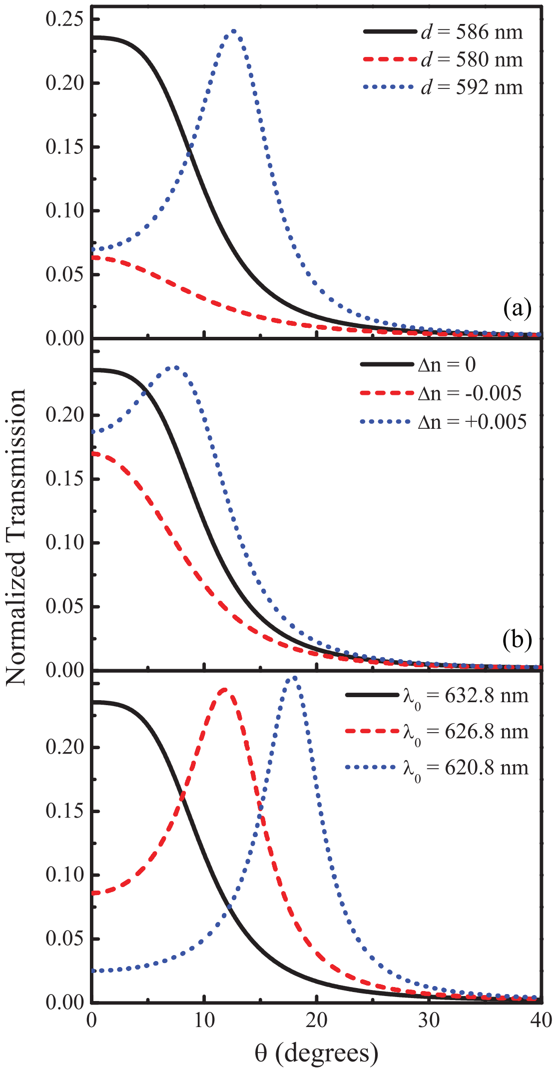

FIG. 8. (Color online) Normalized angular transmission profiles with respect to (a) the thickness and (b) the refractive index change of the PMMA core layer at the illumination wavelength of 632.8 nm. (c) Normalized angular transmission profiles for a small variation of the illumination wavelength (∼1%). A silver layer with a 40-nm thickness was chosen as the aperture and top metal layers. The thickness of the PMMA core in (b) and (c) is 586 nm, as shown in Fig. 7.

PMMA core as shown in Fig. 8(a). In the case of on-axis emission condition, the transmission peak shifts from 0° to around 13° as the thickness of the PMMA core increases about 1%, whereas the transmission peak value is reduced to about one-third as the thickness of the PMMA core decreases about 1%. A similar result was obtained by changing the refractive index of the dielectric core layer as plotted in Fig. 8(b). From these results, we stress that our beaming concept is applicable to on-off switching as well as the DSE. We also calculated in Fig. 8(c) the DSE property with regard to a small variation of the wavelength (∼1%). The transmission angle increases as the wavelength of the incident light decreases. While the separation between the peaks decreases, we see that the DSE in the MDM structure is very sensitive to wavelength variation.

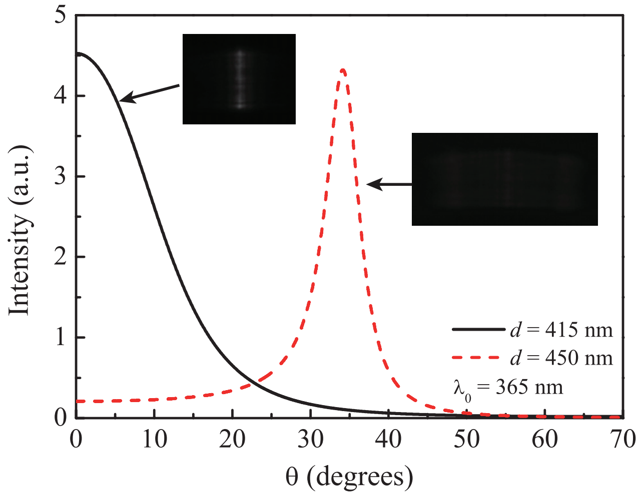

FIG. 9. (Color online) Angular transmission profiles for TE polarization at the 365-nm wavelength ($d = 415$ nm and 450 nm). Measured optical images show the DSE by changing the thickness of the PMMD core as described in the insets.

C. Polarization effect

Our MDM structures are also polarization insensitive, unlike the conventional corrugation-based beaming structures, because the MDM structures also support the RWMs for the transverse electric (TE) polarization.[32] We obtained the angular transmission profile of the same structure with Fig. 4(a) for TE polarization as displayed in Fig. 9. The inset images of Fig. 9 show the optical images of the transmitted light through the MDM structure, indicating that our beaming concept is applicable for both polarizations. The polarization-independent DSE suggests the possibility of manipulating TE-polarized sources through the subwavelength apertures.

V. CONCLUSION

We have presented the RWM-mediated DSE in the MDM structure with a subwavelength aperture for both TM and TE polarization. The MDM structure was able to produce directional emission and small angular divergence. Numerical analysis and experimental results of the RWMs for the MDM structures indicate that the thicknesses of the dielectric core layer and top metal layer play important roles in controlling the divergence angle and emission direction. We emphasize that our MDM structure provides rich options of modulating the directional emission phenomenon by using thermal expansion and thermo/electro-optic effects of the dielectric core layer. In addition, our beaming concept is also applicable to the spatial and spectral emission control of nanoscale light sources embedded in the dielectric layer between two metal films and, for example, can provide new possibilities for high-sensitivity recognition of dye molecules with random positions and orientations.[11,12]

ACKNOWLEDGMENTS

This research was supported by Basic Science Research Program through the National Research Foundation of Korea (NRF) funded by the Ministry of Education, Science and

Technology (2012R1A1A2040714) and Center for Integrated Smart Sensors funded by the Ministry of Education, Science and Technology as Global Frontier Project (CISS-2011-0031864).

---

[*] Corresponding author: ksyu@kaist.edu

[1] H. A. Bethe, Phys. Rev. **66**, 163 (1944).

[2] H. J. Lezec, A. Degiron, E. Devaux, R. A. Linke, L. Martin-Moreno, F. J. Garcia-Vidal, and T. W. Ebbesen, Science **297**, 820 (2002).

[3] P. Kramper, M. Agio, C. M. Soukoulis, A. Birner, F. Muller, R. B. Wehrspohn, U. Gosele, and V. Sandoghdar, Phys. Rev. Lett. **92**, 113903 (2004).

[4] L. Martin-Moreno, F. J. Garcia-Vidal, H. J. Lezec, A. Degiron, and T. W. Ebbesen, Phys. Rev. Lett. **90**, 167401 (2003).

[5] F. I. Baida, D. V. Labeke, and B. Guizal, Appl. Opt. **42**, 6811 (2003).

[6] S. S. Akarca-Biyikli, I. Bulu, and E. Ozbay, Appl. Phys. Lett. **85**, 1098 (2004).

[7] L. B. Yu, D. Z. Lin, Y. C. Chen, Y. C. Chang, K. T. Huang, J. W. Liaw, J. T. Yeh, J. M. Liu, C. S. Yeh, and C. K. Lee, Phys. Rev. B **71**, 041405(R) (2005).

[8] D. Z. Lin, C. K. Chang, Y. C. Chen, D. L. Yang, M. W. Lin, J. T. Yeh, J. M. Liu, C. Kuan, C. S. Yeh, and C. K. Lee, Opt. Express **14**, 3503 (2006).

[9] T. Ishi, J. Fujikata, K. Makita, T. Baba, and K. Ohashi, Jpn. J. Appl. Phys. **44**, L364 (2005).

[10] H. Aouani, O. Mahboub, N. Bonod, E. Devaux, E. Popov, H. Rigneault, T. W. Ebbesen, and J. Wenger, Nano Lett. **11**, 637 (2011).

[11] Y. C. Jun, K. C. Y. Huang, and M. L. Brongersma, Nat. Commun. **2**, 283 (2011).

[12] H. Aouani, O. Mahboub, E. Devaux, H. Rigneault, T. W. Ebbesen, and J. Wenger, Nano Lett. **11**, 2400 (2011).

[13] N. F. Yu, J. Fan, Q. J. Wang, C. Pflúgl, L. Diehl, T. Edamura, M. Yamanishi, H. Kan, and F. Capasso, Nat. Photon. **2**, 564 (2008).

[14] B. Guo, G. Song, and L. Chen, Appl. Phys. Lett. **91**, 021103 (2007).

[15] C. Genet and T. W. Ebbesen, Nature **445**, 39 (2007).

[16] K. G. Lee, X. W. Chen, H. Eghlidi, P. Kukura, R. Lettow, A. Renn, V. Sandoghdar, and S. Götzinger, Nat. Photon. **5**, 166 (2011).

[17] X. W. Chen, S. Götzinger, and V. Sandoghdar, Opt. Lett. **36**, 3545 (2012).

[18] S. Enoch, G. Tayeb, P. Sabouroux, N. Guerin, and P. Vincent, Phys. Rev. Lett. **89**, 213902 (2002).

[19] H. Liu and K. J. Webb, Phys. Rev. B **81**, 201404(R) (2010).

[20] J. B. Pendry, A. J. Holden, W. J. Stewart, and I. Youngs, Phys. Rev. Lett. **76**, 4773 (1996).

[21] V. A. Podolskiy and E. E. Narimanov, Phys. Rev. B **71**, 201101(R) (2005).

[22] B. Wood, J. B. Pendry, and D. P. Tsai, Phys. Rev. B **74**, 115116 (2006).

[23] C. Reale, Infrared Phys. **10**, 175 (1970).

[24] M. Yano, M. Fukui, M. Haraguchi, and Y. Shintani, Surf. Sci. **227**, 129 (1990).

[25] W.-J. Lee, J.-E. Kim, H. Y. Park, S. Park, M. s. Kim, J. T. Kim, and J. J. Ju, J. Appl. Phys. **103**, 073713 (2008).

[26] J. J. Burke, G. I. Stegeman, and T. Tamir, Phys. Rev. B **33**, 5186 (1986).

[27] D. O. S. Melville and R. J. Blaikie, Physica B **394**, 197 (2007).

[28] E. Palik, *Handbook of Optical Constants of Solids* (Academic Press, New York, 1985).

[29] S. N. Kasarova, N. G. Sultanova, C. D. Ivanov, and I. D. Nikolov, Opt. Mater. **29**, 1481 (2007).

[30] M. A. Gilmore and B. L. Johnson, J. Appl. Phys. **93**, 4497 (2003).

[31] J. Chen, G. A. Smolyakov, S. R. J. Brueck, and K. J. Malloy, Opt. Express **16**, 14902 (2008).

[32] S. Hayashi, A. Maekawa, S. C. Kim, and M. Fujii, Phys. Rev. B **82**, 035441 (2010).

[33] S. Park, M. s. Kim, J. J. Ju, J. T. Kim, S. K. Park, J.-M. Lee, W.-J. Lee, and M.-H. Lee, Opt. Commun. **283**, 3267 (2010).

[34] G. Ghosh, *Handbook of Thermo-Optic Coefficients of Optical Materials with Applications* (Academic Press, San Diego, 1998).

[35] B. Yates, *Thermal Expansion* (Plenum Press, New York, 1972).

[36] R. W. Boyd, *Nonlinear Optics*, 2nd ed. (Academic Press, New York, 2003).

[37] R. A. Soref and B. R. Bennett, IEEE J. Quantum Electron. **23**, 123 (1987).